

Anomalous Localization and Mobility Edges in Non-Hermitian Quasicrystals with Disordered Imaginary Gauge Fields

Guolin Nan

Sanli Honors College, School of Physics and Electronics Engineering, Shanxi University, Taiyuan 030006, China

Zhijian Li

Sanli Honors College, School of Physics and Electronics Engineering, Shanxi University, Taiyuan 030006, China and

Institute of Theoretical Physics and State Key Laboratory of Quantum Optics Technologies and Devices, Shanxi University, Taiyuan 030006, China

Feng Mei

State Key Laboratory of Quantum Optics Technologies and Devices,

Institute of Laser Spectroscopy, Shanxi University, Taiyuan 030006, China

Zhihao Xu^{*}

Institute of Theoretical Physics and State Key Laboratory of Quantum

Optics Technologies and Devices, Shanxi University, Taiyuan 030006, China

(Dated: January 22, 2026)

We study anomalous localization in a one-dimensional non-Hermitian quasicrystal with a spatially disordered imaginary gauge field. The system is a generalized Aubry-André-Harper (AAH) chain with asymmetric nearest- and next-nearest-neighbor hoppings generated by a Bernoulli imaginary gauge field and a quasiperiodic onsite potential. In the standard non-Hermitian AAH limit, the system undergoes a transition from a fully erratic non-Hermitian skin effect (ENHSE) phase to a fully localized phase. We show that the fractal dimension cannot distinguish these phases, whereas the Lyapunov exponent and center-of-mass fluctuations provide sharp diagnostics. This transition is accompanied by a complex-to-real spectral change under periodic boundary conditions and a topological change of the spectral winding number. With next-nearest-neighbor hopping, we uncover an anomalous mobility edge separating Anderson-localized states from ENHSE states, rather than extended states. This mobility edge is captured by an energy-dependent winding number that vanishes in the localized regime. Finally, we propose a dynamical probe based on wave-packet expansion: for typical disorder realizations, the dynamics shows winding-controlled drift and disorder-selected pinning or boundary-wrapping recurrence, while disorder averaging restores Hermitian-like transport. These results offer practical spectral, topological, and dynamical diagnostics of anomalous localization and mobility edges in non-Hermitian quasicrystals.

^{*} xuzhihao@sxu.edu.cn

INTRODUCTION

Non-Hermitian quantum systems arise in many open and driven platforms, where gain and loss [1–9], dissipation [9–15], or effective non-unitary evolution [16–20] are present. Typical examples include photonics [21–25], acoustics [7, 16, 26–28], electrical circuits [29–33], and engineered quantum devices [21, 34–38]. Non-Hermiticity can also come from non-reciprocal couplings [14, 21, 36, 39–41] and continuous measurement or monitored dynamics [12, 30, 31, 42–45]. In these settings, complex energy spectra [46–50], amplification or attenuation [35, 51–53], and sensitivity to boundary conditions [34, 54–56] often lead to physics that has no Hermitian counterpart.

A central phenomenon enabled by non-Hermiticity is the non-Hermitian skin effect (NHSE): under open boundary conditions (OBCs), a macroscopic number of eigenstates accumulate near the boundaries [41, 54, 57–67]. This accumulation invalidates the usual bulk-boundary correspondence based on Bloch bands [60, 68–71], and motivates non-Bloch descriptions and topological characterizations in the complex-energy plane [34, 39–41, 44–46, 60, 69, 72, 73]. When non-Hermiticity is combined with aperiodic order, such as quasiperiodic lattices and quasicrystals, the interplay among interference, quasiperiodic modulation, and non-reciprocity can generate rich phase diagrams, including localization transitions and changes of spectral winding [74–78].

Quasiperiodic models provide a route to localization physics without fully random disorder. The Aubry-André-Harper (AAH) model is a paradigmatic example, featuring a sharp delocalization-localization transition tuned by the strength of an incommensurate onsite modulation [79–83]. When longer-range hopping is included, generalized AAH models support mobility edges, namely energy-dependent boundaries that separate localized and extended states [84, 85]. These Hermitian results motivate the question of how mobility-edge physics is reshaped in non-Hermitian quasicrystals, especially when the non-Hermiticity is not spatially uniform.

Another basic issue concerns the relation between spectral localization and dynamics. In Hermitian disordered systems, exponential localization of eigenstates is tied to the suppression of transport [86, 87]. However, in non-Hermitian systems this relation can be altered. Recent experiments and theory have shown that wave propagation can remain possible even when all eigenstates are exponentially localized, leading to unusual spreading that are controlled by the distribution of imaginary parts of eigenenergies [33, 39, 72, 88–90]. These results highlight that non-Hermitian systems may display nontrivial dynamics in regimes where a Hermitian system would be dynamically localized. This motivates a careful, phase-resolved study that combines eigenstate diagnostics, spectral topology, and real-time evolution.

A particularly interesting and less explored direction appears when an imaginary gauge field becomes spatially disordered [91–96]. In this case, non-reciprocity varies from bond to bond and cannot be described by a single uniform asymmetry. Recently, Longhi uncovered that a disordered imaginary gauge field can induce an “erratic” non-Hermitian skin effect (ENHSE) [97]: instead of accumulating at a boundary as in the conventional NHSE, eigenstates show macroscopic accumulation around seemingly irregular bulk positions selected by the disorder realization. This phenomenon poses a challenge for localization characterization. On the one hand, both ENHSE states and conventional Anderson-localized states are spatially confined, and their fractal dimensions can vanish in the thermodynamic limit. On the other hand, their physical origins and spectral and topological properties can be very different. It is therefore important to identify practical diagnostics that can distinguish these phases and to clarify whether a mobility edge can separate two distinct types of localized states, rather than separating extended and localized states as in the Hermitian case.

In this work, we address these questions in a one-dimensional (1D) non-Hermitian quasicrystal described by a generalized AAH chain with a Bernoulli-type disordered imaginary gauge field and a quasiperiodic onsite modulation. Our model includes both nearest-neighbor (NN) and next-nearest-neighbor (NNN) hoppings, allowing us to study both the standard AAH limit and mobility-edge physics in a unified setting. We uncover anomalous localization behavior that links real-space accumulation, spectral reality, and complex-energy topology. For the standard non-Hermitian AAH limit, we find a transition from a fully ENHSE phase to a conventional fully localized phase. We show that the fractal dimension fails to distinguish these phases, while the Lyapunov exponent provides a sharp criterion. We further introduce a diagnostic based on fluctuations of eigenstate centers of mass, which clearly separates macroscopic ENHSE accumulation from conventional localization. This transition is accompanied by a complex-to-real spectral change under periodic boundary conditions (PBCs) and a change of spectral winding from nontrivial to trivial. When weak NNN hopping is included, we demonstrate the emergence of an anomalous mobility edge. Different from the Hermitian case, this mobility edge separates Anderson-localized states from ENHSE-type states, rather than separating extended and localized ones. We show that this boundary can be captured by an energy-dependent winding number that becomes trivial in the Anderson-localized sector. Finally, we propose a dynamical detection scheme based on wave-packet evolution: for typical disorder realizations, the wave packet displays winding-controlled drift and disorder-selected pinning or boundary-wrapping recurrence, whereas disorder-averaged dynamics restores Hermitian-like transport behavior. Our results provide a practical route to diagnose anomalous localization and mobility edges in non-Hermitian quasicrystals using complementary spectral, topological, and dynamical observables.

MODEL AND HAMILTONIAN

We consider a 1D non-Hermitian quasicrystal with a spatially disordered imaginary gauge field. This system is described by the non-Hermitian tight-binding Hamiltonian

$$\hat{H} = \sum_j (J_j^L \hat{c}_j^\dagger \hat{c}_{j+1} + J_j^R \hat{c}_{j+1}^\dagger \hat{c}_j) + \sum_j (\tilde{J}_j^L \hat{c}_j^\dagger \hat{c}_{j+2} + \tilde{J}_j^R \hat{c}_{j+2}^\dagger \hat{c}_j) + \sum_j \lambda_j \hat{c}_j^\dagger \hat{c}_j, \quad (1)$$

where \hat{c}_j (\hat{c}_j^\dagger) annihilates (creates) a particle at site j . Here $J_j^{L(R)}$ denote the left (right) NN hopping amplitudes, while $\tilde{J}_j^{L(R)}$ denote the left (right) NNN hopping amplitudes. A spatially disordered imaginary gauge field is implemented via the asymmetric hoppings $J_j^L = J_1 \exp(-h_j)$, $J_j^R = J_1 \exp(h_j)$, $\tilde{J}_j^L = J_2 \exp[-(h_j + h_{j+1})]$, and $\tilde{J}_j^R = J_2 \exp(h_j + h_{j+1})$, where h_j is a Bernoulli random variable taking values $\pm \Delta h$ with equal probability. The quasiperiodic onsite potential is chosen as $\lambda_j = \lambda \cos(2\pi\alpha j)$, where λ is the modulation strength and α is an irrational number characterizing the incommensurate structure.

In the Hermitian limit ($\Delta h = 0$), the model reduces to a generalized AAH model. When the NNN hopping is switched off ($J_2 = 0$), one recovers the standard AAH model, which exhibit a global delocalized-localized transition at $\lambda = 2J_1$. In this case, all the eigenstates are extended for $\lambda < 2J_1$, while all the eigenstates become localized for $\lambda > 2J_1$. When weak NNN coupling is present $J_2 \neq 0$, the generalized AAH model no longer shows a single global transition. Instead, an energy-dependent mobility edge emerges, separating localized and extended states. For $J_2 \ll J_1$, the mobility edge is given by [84, 85]

$$E_c = \frac{1}{2} \lambda \left(\frac{J_1}{J_2} + \frac{J_2}{J_1} \right) - \frac{J_1^2}{J_2}. \quad (2)$$

By varying λ , the system undergoes a sequence of localization transitions, from a fully extended phase to an intermediate phase with coexisting localized and extended states, and finally to a fully localized phase.

In the non-Hermitian case ($\Delta h \neq 0$) for $\lambda = 0$, the disordered imaginary gauge field can induce an ENHSE [97]. This behavior is distinct from both the conventional NHSE, where eigenstates accumulate at one boundary, and Anderson localization, where localized states are distributed throughout the lattice without macroscopic boundary accumulation. In the ENHSE regime, eigenstates exhibit macroscopic localization around seemingly irregular positions in the bulk, typically featuring a dominant localization peak accompanied by possible satellite peaks whose locations depend sensitively on the specific disorder realization. From a characterization perspective, both NHSE and Anderson localization can display a positive Lyapunov exponent $\gamma > 0$ and a vanishing fractal dimension $D = 0$. In contrast, in the ENHSE regime all eigenstates display $\gamma = 0$ while still having $D = 0$, highlighting its unconventional nature compared with standard non-Hermitian skin and Anderson-localized phases.

In the following, we investigate anomalous localization transitions in the generalized non-Hermitian AAH model for the two cases $J_2 = 0$ and $J_2 \neq 0$. Throughout, we set $J_1 = 1$ as the energy unit. Without loss of generality, we fix $\alpha = (\sqrt{5} - 1)/2$ and $\Delta h = 0.5$. Moreover, unless explicitly stated, all numerical results are obtained for a single disorder realization.

ANOMALOUS LOCALIZATION TRANSITIONS

We begin with the non-Hermitian AAH model in Eq. (1) with $J_2 = 0$, which exhibits an anomalous localization transition from a fully ENHSE phase to a fully localized phase. Figure 1 shows the profiles $|\psi_j^{(n)}|$ of ten randomly selected eigenstates for a representative imaginary gauge field realization at different λ and under different boundary conditions, where n is the index of energy level. For weak quasiperiodic modulation [$\lambda = 1$; Figs. 1(a) and 1(c)], these eigenstates display macroscopic accumulation around seemingly irregular bulk locations under both PBCs and OBCs. Typically, each eigenstate features a dominant peak accompanied by some subleading satellite peaks, which is characteristic of the fully ENHSE phase. In contrast, for strong modulation [$\lambda = 3$; Figs. 1(b) and 1(d)], the eigenstates become strongly localized, with localization centers distributed throughout the lattice under both boundary conditions, indicating a conventional fully localized phase. Notably, the spatial structures of the eigenstates in our model with a Bernoulli-type imaginary gauge field are largely insensitive to the boundary conditions: both the accumulation patterns in the fully ENHSE regime and the distribution of localization centers in the fully localized regime remain qualitatively similar under PBCs and OBCs. Motivated by this robustness, we focus on PBCs in the following discussion for clarity.

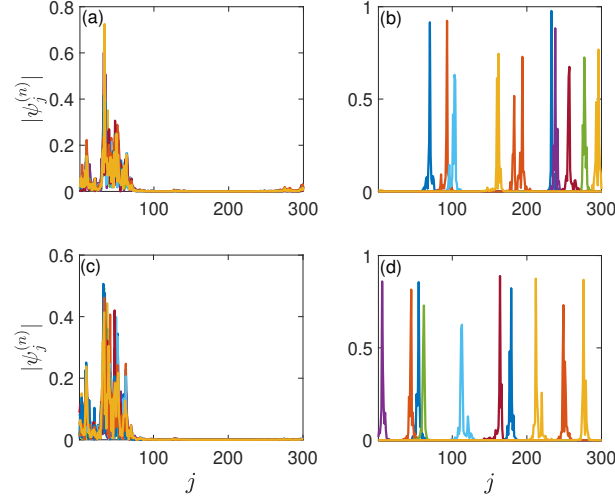


FIG. 1. Representative eigenstate profiles $|\psi_j^{(n)}|$ of the non-Hermitian AAH model [Eq. (1)] with $J_2 = 0$ and $N = 300$ for a fixed imaginary gauge-field realization. Ten randomly chosen eigenstates are shown under PBCs [(a) $\lambda = 1$; (b) $\lambda = 3$] and OBCs [(c) $\lambda = 1$; (d) $\lambda = 3$].

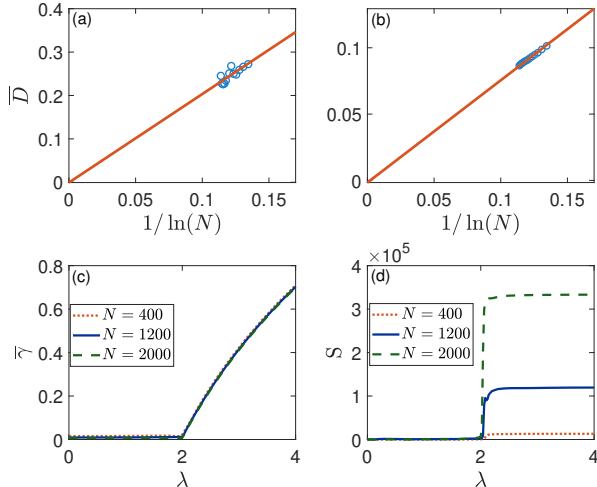


FIG. 2. Mean fractal dimension \overline{D} versus $1/\ln N$ at (a) $\lambda = 1$ and (b) $\lambda = 3$, extrapolating to $\overline{D} \rightarrow 0$ in both phases. (c) Mean Lyapunov exponent $\bar{\gamma}$ as a function of λ for different N , showing $\bar{\gamma} \rightarrow 0$ for $\lambda < 2$ and finite $\bar{\gamma}$ for $\lambda > 2$. (d) Center-of-mass fluctuation S versus λ for different system sizes N , scaling as $S = O(1)$ in the fully ENHSE phase and $S = O(N)$ in the fully localized phase, with a sharp change at $\lambda = 2$. Here, $J_2 = 0$ and all data are obtained for a single realization of the imaginary gauge field.

To quantitatively distinguish the fully ENHSE phase from the fully localized phase, we examine both the fractal dimension and the Lyapunov exponent. The spatial fractal property of an eigenstate $\psi^{(n)}$ with eigenvalue E_n is quantified by the fractal dimension

$$D_n = - \lim_{N \rightarrow \infty} \left[\frac{\ln \text{IPR}^{(n)}}{\ln N} \right], \quad (3)$$

where the inverse participation ratio (IPR) is $\text{IPR}^{(n)} = \sum_j |\psi_j^{(n)}|^4$ and N is the system size. According to Ref. [97], D_n is expected to vanish in the thermodynamic limit for both the fully ENHSE and fully localized phases. Consistent with this, Figs. 2(a) and 2(b) plot the mean fractal dimension $\overline{D} = (1/N) \sum_{n=1}^N D_n$ as a function of $1/\ln N$ for $\lambda = 1$

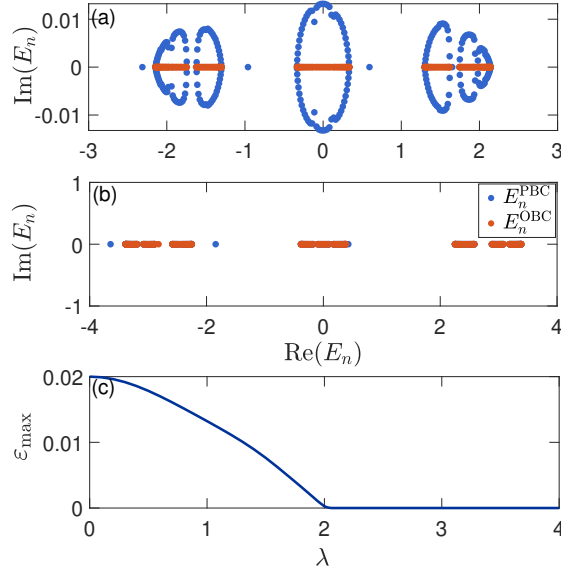


FIG. 3. Eigenenergy spectra under PBCs and OBCs at (a) $\lambda = 1$ and (b) $\lambda = 3$. (c) Maximum imaginary part of the eigenenergies under PBCs ε_{\max} versus λ . Here, $J_2 = 0$, $N = 300$, and all data are obtained for a representative realization of the imaginary gauge field.

and $\lambda = 3$, respectively. In both cases, \overline{D} decreases approximately linearly as $1/\ln N$ is reduced and extrapolates to $\overline{D} \rightarrow 0$ in the thermodynamic limit. Therefore, the fractal dimension alone cannot identify the transition. We therefore consider the Lyapunov exponent γ . For each eigenstate, we define

$$\gamma_n = \left| \lim_{j \rightarrow \infty} \frac{1}{j} \ln \left| \frac{\psi_j^{(n)}}{\psi_1^{(n)}} \right| \right|, \quad (4)$$

and the corresponding mean value $\overline{\gamma} = (1/N) \sum_{n=1}^N \gamma_n$. As detailed in Method, the Lyapunov exponent undergoes a transition from zero to finite at $\lambda = 2$ in the thermodynamic limit. Figure 2(c) shows $\overline{\gamma}$ as a function of the quasiperiodic strength λ for different system sizes. One finds that $\overline{\gamma} \rightarrow 0$ for $\lambda < 2$, whereas it becomes finite for $\lambda > 2$ and increases with λ , signaling the onset of exponential localization. Moreover, $\overline{\gamma}$ essentially insensitive to the system size. Combining these diagnostics, we identify a transition from the fully ENHSE phase to the fully localized phase at $\lambda_c = 2$. Although $\overline{D} \rightarrow 0$ in both regimes, $\overline{\gamma}$ changes from vanishing ($\lambda < 2$) to finite ($\lambda > 2$), providing a sharp criterion for the transition.

Furthermore, motivated by the distinct wave-function profiles in Figs. 1(a) and 1(b), we introduce an additional diagnostic based on fluctuations of the eigenstate center of mass. We define

$$S = \frac{1}{N} \sum_{n=1}^N (x_n - \bar{x})^2, \quad (5)$$

where

$$x_n = \frac{\sum_{j=1}^N j |\psi_j^{(n)}|^2}{\sum_{j=1}^N |\psi_j^{(n)}|^2} \quad (6)$$

is the center-of-mass position of the n -th eigenstate, and $\bar{x} = (1/N) \sum_{n=1}^N x_n$ is the mean center-of-mass position averaged over all eigenstates. Fig. 2(d) shows S as a function of λ for different system sizes. In the fully ENHSE phase, for a fixed imaginary-gauge-field realization the eigenstates share similar skin-accumulated profiles. As a result, their centers of mass cluster around a few preferred bulk locations and the fluctuation remains small, *i.e.*, $S = O(1)$ with weak size dependence. By contrast, in the fully localized phase the localization centers are pinned by disorder and are approximately uniformly distributed along the entire lattice, leading to a fluctuation that grows with system

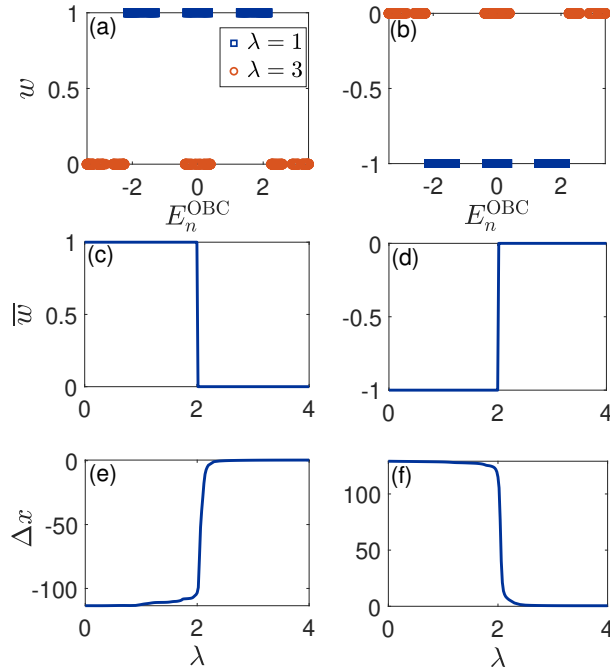


FIG. 4. (a,b) Winding number w evaluated for each reference energy $E_B = E_n^{\text{OBC}}$ at $\lambda = 1$ and $\lambda = 3$. (c,d) Mean winding number \bar{w} versus λ . (e,f) Averaged center-of-mass shift Δx versus λ . Here, $J_2 = 0$ and $N = 300$. The left and right columns correspond to two representative realizations of the imaginary gauge field, for which the winding number in the fully ENHSE phase is $w = 1$ and $w = -1$, respectively.

size, $S = O(N)$. Accordingly, S exhibits a pronounced jump at $\lambda = 2$, consistent with the transition identified from $\bar{\gamma}$.

Many non-Hermitian extensions of the AAH model have been explored, with particular emphasis on the interplay between the complex-to-real spectral transition and the localization transition. Figures 3(a) and 3(b) show the energy spectra for a finite system of size $N = 300$ under different boundary conditions at $\lambda = 1$ and $\lambda = 3$, respectively, for a representative single disorder realization. For $\lambda = 1$ in the fully ENHSE phase [Fig. 3(a)], the spectrum E_n^{PBC} is generally complex under PBCs, whereas under OBCs the spectrum E_n^{OBC} becomes purely real. By contrast, in the fully localized phase [Fig. 3(b)], the spectra under both PBCs and OBCs are entirely real. To quantify the spectral transition, Fig. 3(c) shows the maximum imaginary part of the eigenenergies, $\varepsilon_{\text{max}} = \max[\text{Im}(E_n)]$, as a function of λ under PBCs. For $\lambda < 2$, ε_{max} is finite and decreases gradually as λ increases. When $\lambda > 2$, ε_{max} vanishes, indicating that the PBC spectrum becomes entirely real. This complex-to-real spectral transition occurs at the same critical point as the anomalous localization transition identified above, revealing a direct correspondence between spectral reality and the localization properties of the system. Notably, for a finite system size, the spatial average of the imaginary gauge field, defined as $\bar{h} = (1/N) \sum_{l=1}^N h_l$, typically deviates from zero for a given disorder realization. This finite \bar{h} generically yields a nonzero imaginary part of the spectrum under PBCs in the ENHSE regime. As shown in Appendix A, upon increasing N the average \bar{h} approaches zero and the corresponding ε_{max} tends to zero under PBCs in the thermodynamic limit.

Unlike the Hermitian case, our non-Hermitian AAH model at finite system size can exhibit a topological phase transition in the complex energy plane [75–77]. To characterize the spectral topology, we employ the winding number w , defined as [73, 76, 96]

$$w = \int_0^{2\pi} \frac{d\varphi}{2\pi i} \partial_\varphi \ln \det \left[\hat{H}(\varphi) - E_B \right], \quad (7)$$

where $\hat{H}(\varphi)$ is the Hamiltonian given in Eq. (1) under PBCs with a flux φ threaded through the ring, and E_B is a reference energy. The winding number counts how many times the complex PBC spectrum winds around E_B as φ is varied from 0 to 2π . In our calculations, we take the OBC eigenenergies E_n^{OBC} as reference energies and evaluate w

for each $E_B = E_n^{\text{OBC}}$. Figure 4(a) shows w as a function of E_n^{OBC} for $\lambda = 1$ and $\lambda = 3$ for a representative realization of the imaginary gauge field. For $\lambda = 1$ in the fully ENHSE regime, the PBC spectral trajectory winds around each reference energies E_n^{OBC} , yielding a nontrivial winding number $w = +1$. By contrast, in the fully localized regime ($\lambda = 3$), the spectrum no longer winds around any E_n^{OBC} , and the winding number becomes trivial, $w = 0$, for all reference energies. To summarize the overall topological response, we further compute the mean winding number \bar{w} by averaging w over all reference energies E_n^{OBC} , and plot \bar{w} versus λ in Fig. 4(c). For the finite system size considered and the chosen disorder realization, \bar{w} remains pinned at $+1$ for $\lambda < 2$, and then abruptly drops to $\bar{w} = 0$ when $\lambda > 2$, signaling a topological transition. This behavior is consistent with the complex-to-real spectral transition and the localization transition discussed above. We emphasize that the sign of \bar{w} in the fully ENHSE regime can depend on the specific disorder realization: for other disorder configurations, the nontrivial winding w may switch from $+1$ to -1 , as exemplified in Fig. 4(b) and the corresponding \bar{w} in Fig. 4(d). Nevertheless, upon increasing λ into the fully localized regime, the mean winding number robustly becomes trivial, $\bar{w} = 0$.

We further find that the sign of the mean winding number \bar{w} is closely correlated with the position of the center of mass. Figures 4(e) and (f) show the averaged center-of-mass shift, $\Delta x = \bar{x} - (N + 1)/2$, as a function of λ , where the realizations of the imaginary gauge field are chosen to be the same as those used in Figs. 4(a) and 4(b), respectively. For the realization with $\bar{w} = +1$ shown in Fig. 4(e), the mean center of mass resides in the left half of the chain throughout the fully ENHSE regime: $\Delta x < 0$ and depends only weakly on λ . Once the system enters the fully localized regime ($\lambda > 2$), Δx displays a sharp crossover and rapidly approaches $\Delta x \simeq 0$, indicating that the localized states are nearly uniformly distributed along the lattice. Conversely, for the realization with $\bar{w} = -1$ shown in Fig. 4(f), the center of mass is locked on the opposite side in the fully ENHSE regime, with $\Delta x > 0$ remaining almost unchanged as λ increases, reflecting a robust accumulation on the right side dictated by the corresponding imaginary-gauge configuration. When $\lambda > 2$, Δx again abruptly drifts toward zero and eventually saturates around $\Delta x \simeq 0$ in the fully localized phase. These results show that the sign of the mean winding number \bar{w} determines the sign of the center-of-mass shift Δx , and thus fixes which side of the chain the center of mass resides in within the ENHSE regime. When \bar{w} becomes trivial ($\bar{w} = 0$), the bias disappears and $\Delta x \rightarrow 0$, reflecting the disappearance of spectral winding concomitant with the loss of skin-induced accumulation in the localized regime.

ANOMALOUS MOBILITY EDGES

Having established the anomalous transition in the standard non-Hermitian AAH limit ($J_2 = 0$), we now turn to the case with weak NNN coupling ($J_2 \neq 0$ with $J_2 \ll J_1$) to demonstrate the emergence of anomalous mobility edges. In the absence of the imaginary gauge field, the Hermitian generalized AAH model exhibits a conventional mobility edge, whose analytical form is given by Eq. (2). Remarkably, in the presence of the imaginary gauge field, the non-Hermitian model still supports a mobility edge located at the same $E_c(\lambda)$ as in the Hermitian case (see Methods for details). The mobility edge is nevertheless anomalous here, because it separates conventional Anderson-localized states from ENHSE-type states with macroscopic accumulation at irregular bulk positions, rather than separating extended and localized states as in the Hermitian setting. In the following calculation, we fix $J_2 = 0.1$.

Consistent with our analysis for $J_2 = 0$, we find that the fractal dimension is not a reliable order parameter for charting the phase diagram in this non-Hermitian setting. We therefore quantify localization using the Lyapunov exponent and employ it to construct the phase diagram. Figure 5(a) presents the localization phase diagram under PBCs as a function of the quasiperiodic modulation strength λ and the real part of the eigenenergy $\text{Re}(E_n^{\text{PBC}})$, obtained for a representative realization of the imaginary gauge field. The color encodes the Lyapunov exponent of eigenstates at different energies, and the black dashed line marks the anomalous mobility edge predicted by Eq. (2). For $\lambda < \lambda_{c1} = 1.5$, the system is in the fully ENHSE phase. As illustrated in Fig. 5(b) for $\lambda = 1$, ten randomly chosen PBC eigenstate profiles $|\psi_j^{(n)}|$ display pronounced macroscopic accumulation around irregular bulk positions, accompanied by weaker satellite peaks. For $\lambda > \lambda_{c2} = 2.5$, the system enters the fully localized phase, where eigenstate remain localized but their localization centers are distributed nearly uniformly along the chain, as shown in Fig. 5(c) for $\lambda = 3$ (ten randomly chosen eigenstates). In the intermediate window $\lambda_{c1} < \lambda < \lambda_{c2}$, an anomalous mobility edge emerges in the $(\text{Re}(E_n^{\text{PBC}}), \lambda)$ plane and separates Anderson-localized states from ENHSE-type states. Taking $\lambda = 1.9$ as an example, the mobility edge occurs at $E_c \simeq -0.4$. Eigenstate with $\text{Re}(E_n^{\text{PBC}}) < E_c$ display conventional Anderson-localization features [Fig. 5(d), ten randomly chosen eigenstates], whereas those with $\text{Re}(E_n^{\text{PBC}}) > E_c$ show ENHSE-type accumulation [Fig. 5(e), ten randomly chosen eigenstates].

To further elucidate the interplay between the anomalous mobility edge and spectral topology, we examine how the energy spectrum and its topological features evolve as λ is varied. Figures 6(a)-6(c) show the energy spectra under different boundary conditions for the same realization of the imaginary gauge field as in Fig. 5, at $\lambda = 1, 1.9$, and 3 , respectively. In the fully ENHSE regime ($\lambda < \lambda_{c1}$), the spectrum splits into well-separated clusters. Under PBCs, the eigenvalues are complex and form loop structures in the complex energy plane, as shown in Fig. 6(a) for $\lambda = 1$. As λ

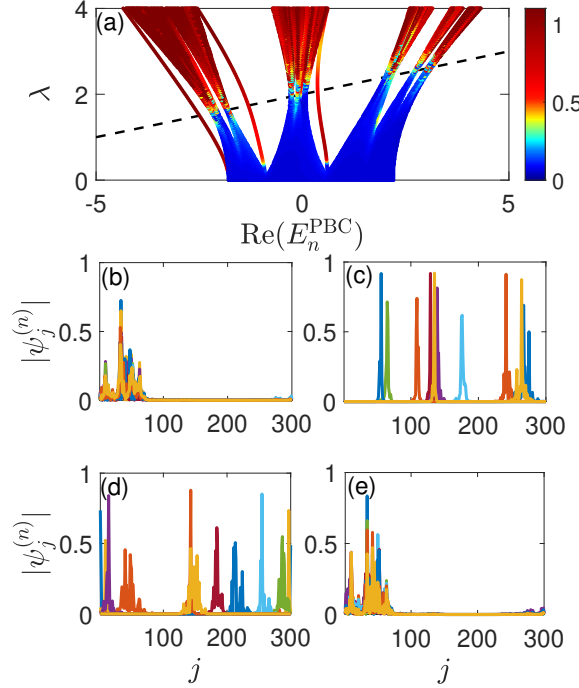


FIG. 5. (a) Localization phase diagram under PBCs in the $(\text{Re}(E_n^{\text{PBC}}), \lambda)$ plane, with color indicating the Lyapunov exponent. The black dashed line marks the anomalous mobility edge $E_c(\lambda)$ from Eq. (2). (b-e) Representative PBC eigenstate profiles $|\psi_j^{(n)}|$ (ten randomly chosen states): (b) $\lambda = 1$, (c) $\lambda = 3$, (d) $\lambda = 1.9$ with $\text{Re}(E_n^{\text{PBC}}) < E_c$, and (e) $\lambda = 1.9$ with $\text{Re}(E_n^{\text{PBC}}) > E_c$. Here, $J_2 = 0.1$ and $N = 300$, and all data are obtained for a representative realization of the imaginary gauge field.

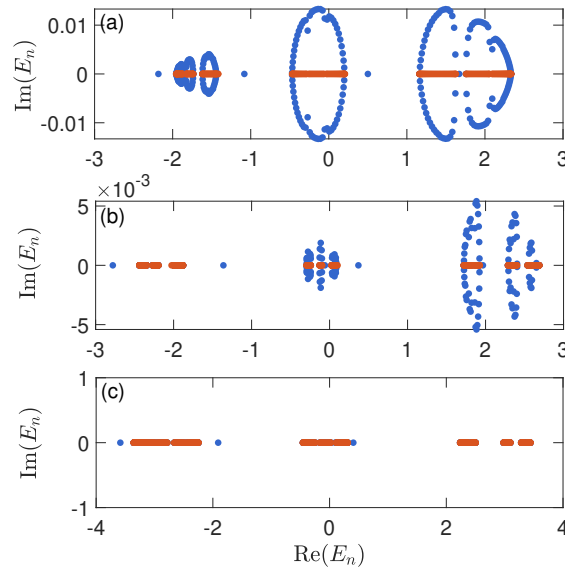


FIG. 6. Energy spectra under different boundary conditions for the same imaginary-gauge-field realization as in Fig. 5, at (a) $\lambda = 1$, (b) $\lambda = 1.9$, and (c) $\lambda = 3$. Here, $J_2 = 0.1$ and $N = 300$.

increases into the intermediate phase (e.g., $\lambda = 1.9$), the spectrum becomes energy-selective across the mobility edge: under PBCs, eigenvalues with $\text{Re}(E_n^{\text{PBC}}) < E_c$ collapse onto the real axis, whereas those with $\text{Re}(E_n^{\text{PBC}}) > E_c$ remain complex and continue to form loops in the complex-energy plane, as shown in Fig. 6(b). Upon further increasing λ into the fully localized regime ($\lambda > \lambda_{c2}$), the entire PBC spectrum becomes purely real, as shown in Fig. 6(c) for $\lambda = 3$. By contrast, under OBCs the spectrum E_n^{OBC} remains purely real for all λ considered. To quantify the complex-to-real spectral transition under PBCs, we plot the maximum imaginary part of the eigenenergies ε_{max} as a function of λ in Fig. 7(a). We find that ε_{max} vanishes at $\lambda \simeq 2.5$, signaling the emergence of an entirely real PBC spectrum. This transition coincides with the localization critical point λ_{c2} .

To directly link the anomalous mobility edge to the spectral topology, we compute the winding number w by taking the OBC eigenenergies E_n^{OBC} as reference points for different λ , as shown in Figs. 7(b)-7(d) for the same realization of the imaginary gauge field as in Fig. 5. In the fully ENHSE regime, the PBC spectrum encircles each reference energy E_n^{OBC} , yielding a nonzero winding number $w = 1$ [Fig. 7(b) for $\lambda = 1$], consistent with the loop structures in the complex-energy plane. As λ increases into the intermediate phase, the winding becomes reference-energy dependent. For $\lambda = 1.9$ in Fig. 7(c), reference energies with $E_n^{\text{OBC}} < E_c$ are no longer enclosed by the PBC loops and hence give $w = 0$, whereas those with $E_n^{\text{OBC}} > E_c$ remain enclosed and retain $w = 1$. Upon further increasing λ into the fully localized regime [e.g., $\lambda = 3$ in Fig. 7(d)], the PBC spectrum collapses onto the real axis, and the winding becomes trivial ($w = 0$) for all E_n^{OBC} . Notably, changing the imaginary-gauge realization may flip the sign of the winding number in the ENHSE regime, whereas the energy-dependent onset of trivial winding across E_c remains unchanged. This provides a direct topological characterization of the anomalous mobility edge.

Our results show that introducing a weak NNN coupling ($J_2 \neq 0$) into the non-Hermitian AAH model gives rise to an anomalous mobility edge. Although its location $E_c(\lambda)$ remains determined by the Hermitian criterion in Eq. (2), it separates Anderson-localized states from ENHSE-type states rather than from extended states. This is corroborated by the Lyapunov exponent, the energy-selective complex-to-real spectral transition under PBCs, and the energy-dependent winding number that becomes trivial across E_c and ultimately vanishes in the fully localized regime.

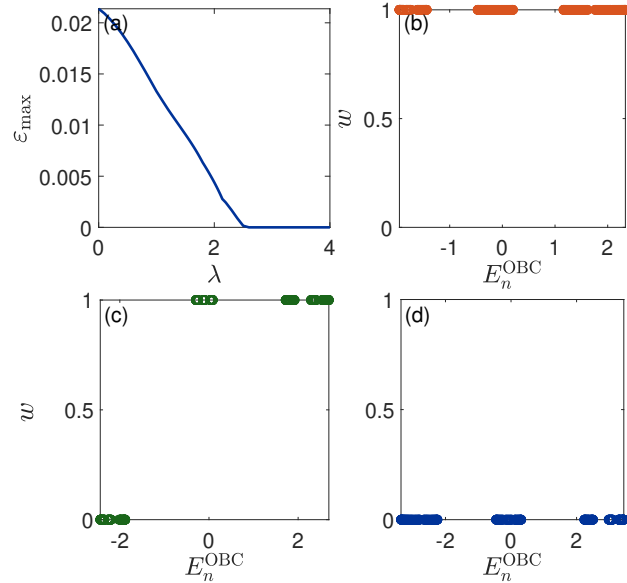


FIG. 7. (a) Maximum imaginary part of PBC eigenenergies ε_{max} versus λ . Winding number w evaluated by taking the OBC eigenenergies E_n^{OBC} as reference energies for (b) $\lambda = 1$, (c) $\lambda = 1.9$, and (e) $\lambda = 3$. Here, $J_2 = 0.1$ and $N = 300$, and the imaginary-gauge-field realization is the same as in Fig. 5.

DYNAMICAL DETECTION

To provide an intuitive picture of the dynamics, we examine the wave-function profile $\rho_j(t) = \langle \Psi(t)|j\rangle\langle j|\Psi(t)\rangle = |\Psi_j(t)|^2$ shown in Fig. 8. Figures. 8(a)-8(c) show results under PBCs for a representative realization of the random imaginary gauge field (the same realization as in Fig. 5), at $\lambda = 1, 1.9$, and 3 , respectively. Figures 8(d)-8(f) show

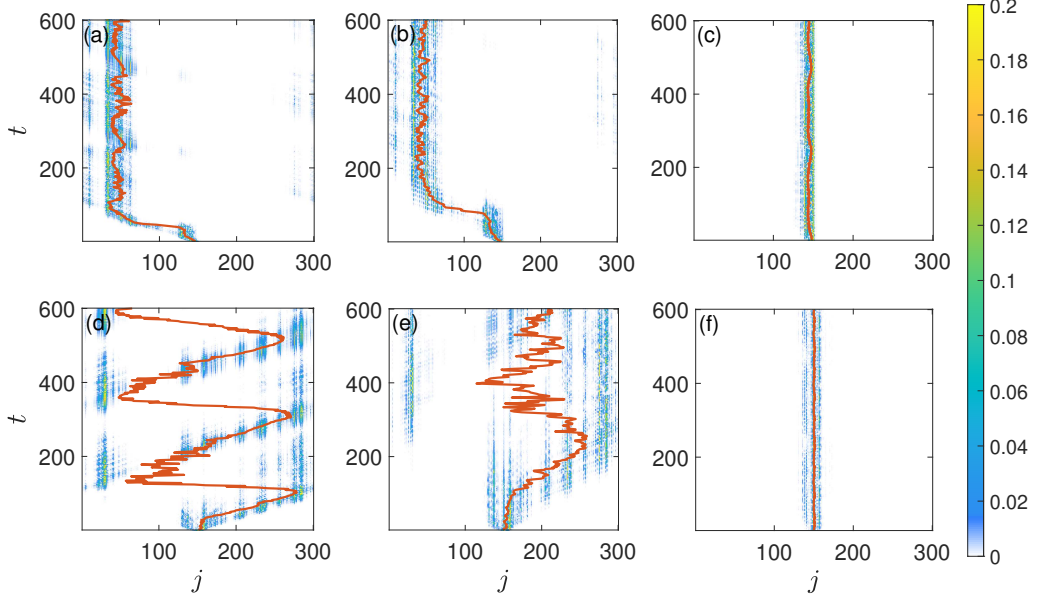


FIG. 8. Time evolution of the wave-function profile $\rho_j(t)$ under PBCs for two representative realizations of the random imaginary gauge field with an initial state $|\Psi(0)\rangle = |j_0\rangle$ and $j_0 = N/2$ (even N). The solid line in each panel denotes the wave-packet center of mass $x(t)$. Panels (a)–(c) correspond to the same realization as in Fig. 5 at $\lambda = 1, 1.9$, and 3 , respectively. Panels (d)–(f) show an alternative realization at the same λ values with opposite winding ($w = -1$) in the ENHSE regime. Here, $J_2 = 0.1$ and $N = 300$.

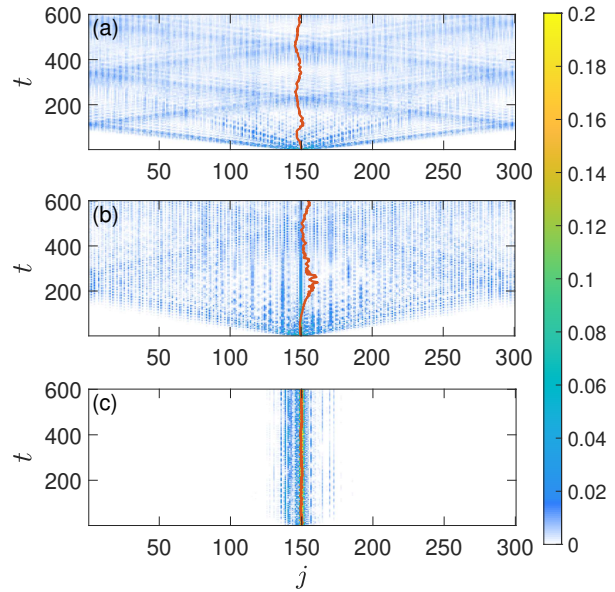


FIG. 9. Disorder-averaged wave-packet dynamics. Disorder-averaged density profile $\bar{\rho}_j(t)$ averaged over $N_c = 1000$ realizations of the imaginary gauge field for (a) $\lambda = 1$, (b) $\lambda = 1.9$, and (c) $\lambda = 3$. Solid lines show the evolution of the disorder-averaged center of mass $\bar{x}(t)$. Here, $J_2 = 0.1$, $N = 300$, and $j_0 = N/2 = 150$.

results under PBCs for a different gauge-field realization at the same three values of λ . This latter realization is chosen such that, in the fully ENHSE regime, the winding numbers associated with all reference energies E_n^{OBC} are $w = -1$, and in the intermediate regime the reference energies satisfying $E_n^{\text{OBC}} > E_c$ correspond to $w = -1$. The solid lines in each panel traces the time evolution of the wave-packet center of mass, $x(t) = \sum_j j \rho_j(t)$, which directly quantifies the transient drift and the subsequent long-time behavior.

For $\lambda = 1$ in Fig. 8(a), the system lies in the fully ENHSE phase, where the winding number associated with all reference energies E_n^{OBC} is $w = 1$. At short times, the initially localized wave packet exhibits a pronounced leftward drift and develops multiple localized peaks, consistent with the macroscopic accumulation positions characteristic of the ENHSE phase; correspondingly, $x(t)$ shifts to the left. At long times, the wave function becomes pinned at well-defined sites, with the specific pinned locations selected by the particular disorder realization of the imaginary gauge field. Accordingly, the center of mass is pinned on the left side of the chain, with small fluctuations. In the intermediate phase with an anomalous mobility edge and reference-energy-dependent winding [Fig. 7(c); e.g., $\lambda = 1.9$ in Fig. 8(b)], the wave packet exhibits a short-time transient near the initial position. It then develops a directional bias induced by the $w = 1$ sector, leading to a leftward drift toward the ENHSE-favored accumulation region. This is captured by the center-of-mass trajectory: $x(t)$ displays an initial plateau near j_0 , followed by a pronounced shift to the left. At long times, the wave packet ultimately localizes at the ENHSE-favored accumulation positions, and $x(t)$ becomes pinned on the left side with small fluctuations. Figure 8(c) shows the case $\lambda = 3$, where the system is in the fully localized phase. Here the wave packet remains localized around the initial site throughout the evolution and exhibits no apparent directional drift, consistent with the fact that all reference energies E_n^{OBC} correspond to a trivial winding $w = 0$. Accordingly, the center of mass stays close to j_0 at all times.

In Fig. 8(d), for the alternative gauge-field realization at $\lambda = 1$ with winding $w = -1$, the wave packet displays a pronounced rightward drift at short times, and the center of mass shifts to the right. Once the wave packet reaches the right boundary, PBCs wrap it around the ring. As a result, $x(t)$ undergoes a rapid leftward jump and subsequently resumes its rightward drift. This boundary-crossing-and-reentry process repeats, producing a recurrent sawtooth-like trajectory of $x(t)$ under PBCs. Correspondingly, the wave-function density does not settle at a single static position; instead, it recurrently accumulates at the ENHSE-favored macroscopic accumulation sites dictated by the disorder configuration, *i.e.*, the dominant high-density ENHSE peaks re-emerge periodically along the ring. In Fig. 8(e) ($\lambda = 1.9$ for the same alternative realization), the wave packet again shows a short-time transient near the initial position before developing a clear rightward bias. When it reaches the right boundary, PBCs wrap it around the ring so that it reappears near the left side, close to the ENHSE-favored accumulation region. This produces a rapid leftward jump of the center of mass, followed by continued rightward drift. Repeating this process leads to a periodic dynamics: $x(t)$ forms a characteristic sawtooth pattern, while the wave-function density recurrently concentrates at the macroscopic ENHSE accumulation sites selected by the disorder realization. After the initial transient, the overall behavior closely resembles that in Fig. 8(d). When the system enters the fully localized phase [Fig. 8(f) with $\lambda = 3$], the dynamics becomes similar to that in Fig. 8(c), with the wave packet remaining localized near the initial site and showing no systematic drift. Overall, for a fixed disorder realization, the short-time dynamics is largely governed by the winding-controlled directional bias: the wave packet develops a robust drift direction (leftward for $w = 1$ and rightward for $w = -1$), and in the intermediate regime this drift is often preceded by a transient plateau near j_0 . By contrast, the long-time behavior is strongly realization dependent: depending on the disorder configuration, the wave packet may become pinned at different ENHSE accumulation sites or exhibit recurrent boundary-crossing dynamics under PBCs, leading to substantial differences across realizations.

While Fig. 8 highlights the realization-specific drift, pinning, and boundary-wrapping dynamics induced by the random imaginary gauge field under PBCs, it is also instructive to examine how these features survive after averaging over disorder. To this end, we compute the disorder-averaged wave-packet evolution and the corresponding averaged center-of-mass motion, shown in Fig. 9. Figures 9(a)–9(c) show the disorder-averaged wave-packet evolution $\bar{\rho}_j(t)$ for $\lambda = 1, 1.9$, and 3, respectively, where the dynamics are averaged over $N_c = 1000$ realizations of the imaginary gauge field. After disorder averaging, the evolution closely resembles that of the Hermitian counterpart [43]. In Fig. 9, the solid line in each panel denotes the time evolution of the disorder-averaged center of mass $\bar{x}(t) = (1/N_c) \sum_{r=1}^{N_c} x_r(t)$, where $x_r(t) = \sum_j j \rho_j^{(r)}(t)$ and $\rho_j^{(r)}(t)$ is the density for the r th realization. For $\lambda = 1$, the system exhibits ballistic transport, and $\bar{x}(t)$ shows no appreciable drift and remains close to the initial position. For $\lambda = 1.9$, part of transport displays ballistic-like spreading, whereas a finite portion remains localized around the initial site; accordingly, $\bar{x}(t)$ still shows no clear drift and stays near its initial value, consistent with mobility-edge-like dynamics in the corresponding Hermitian system [43]. When the system enters the fully localized phase, as in Fig. 9(c) for $\lambda = 3$, both $\bar{\rho}_j(t)$ and $\bar{x}(t)$ remain localized near the initial position throughout the evolution, again in agreement with the disorder-averaged dynamics expected for a Hermitian localized phase.

In short, for individual disorder realizations the short-time dynamics is primarily controlled by the winding, yielding a robust directional bias. However, the long-time behavior is strongly realization dependent, with the pinning or recurrence pattern set by the specific disorder configuration. Upon disorder averaging, these sample-specific ENHSE

signatures are largely washed out and the dynamics reduces to Hermitian-like transport across the extended, intermediate, and localized regimes.

CONCLUSION

We studied anomalous localization in a 1D non-Hermitian quasiperiodic lattice with a spatially disordered imaginary gauge field, focusing on both the standard AAH limit ($J_2 = 0$) and the generalized model with weak NNN hopping ($J_2 \neq 0$). For $J_2 = 0$, we identified an anomalous transition from a fully ENHSE phase to a conventional localized phase at $\lambda_c = 2$: while the fractal dimension extrapolates to $\overline{D} \rightarrow 0$ in both regimes, the Lyapunov exponent and the fluctuation of the center-of-mass provide a sharp distinction. We further showed that this transition is accompanied by a complex-to-real spectral change under PBCs and a winding-number switch from nontrivial to trivial, with the winding sign correlating with the direction of macroscopic accumulation. With weak NNN hopping, we demonstrated an anomalous mobility edge located at the same $E_c(\lambda)$ as in the Hermitian generalized AAH model, but separating Anderson-localized states from ENHSE-type macroscopic-accumulation states rather than extended ones. Finally, wave-packet dynamics under PBCs provides a direct probe: a typical realization exhibits winding-controlled drift and disorder-selected pinning or recurrence, whereas disorder averaging washes out these ENHSE-specific signatures and restores Hermitian-like transport behavior.

METHODS

Lyapunov exponent calculation

For the generalized non-Hermitian AAH model, the stationary Schrödinger equation for an eigenstate $|\psi^{(n)}\rangle$ with energy E_n is given by

$$E_n \psi_j = \tilde{J}_j^L \psi_{j+2}^{(n)} + J_j^L \psi_{j+1}^{(n)} + J_{j-1}^R \psi_{j-1}^{(n)} + \tilde{J}_{j-2}^R \psi_{j-2}^{(n)} + \lambda_j \psi_j^{(n)}, \quad (8)$$

where $\psi_j^{(n)}$ denotes the wave-function amplitude at site j . To characterize the localization nature of the eigenstates, we calculate the Lyapunov exponent $\gamma(E_n)$, defined as

$$\gamma(E_n) = \lim_{j \rightarrow \infty} \frac{1}{j} \ln \left| \frac{\psi_j^{(n)}}{\psi_1^{(n)}} \right|. \quad (9)$$

This quantity measures the asymptotic exponential growth or decay of the wave function.

To analytically determine the phase boundaries, we employ a non-unitary gauge transformation that maps the non-Hermitian Hamiltonian to a Hermitian counterpart. We introduce the transformed basis

$$\psi_j^{(n)} = e^{\sum_{l=1}^{j-1} h_l} \phi_j^{(n)}. \quad (10)$$

Substituting Eq. (10) into Eq. (8) and utilizing the specific forms of the disordered hopping amplitudes [$J_j^L = J_1 e^{-h_j}$, $J_j^R = J_1 e^{h_j}$, $\tilde{J}_j^L = J_2 e^{-(h_j+h_{j+1})}$, and $\tilde{J}_j^R = J_2 e^{(h_j+h_{j+1})}$], the imaginary gauge factors cancel out. The spectral problem is thus mapped onto that of a Hermitian generalized AAH model with hoppings J_1 and J_2 :

$$E_n \phi_j^{(n)} = J_1 (\phi_{j+1}^{(n)} + \phi_{j-1}^{(n)}) + J_2 (\phi_{j+2}^{(n)} + \phi_{j-2}^{(n)}) + \lambda_j \phi_j^{(n)}. \quad (11)$$

By substituting the transformation relation Eq. (10) into the definition of the Lyapunov exponent Eq. (9), we obtain the relation between the Lyapunov exponents of the non-Hermitian system (γ_{NH}) and the auxiliary Hermitian system (γ_{H}):

$$\gamma_{\text{NH}}(E_n) = \left| \lim_{j \rightarrow \infty} \frac{1}{j} \ln \left| \frac{\phi_j^{(n)}}{\phi_1^{(n)}} \right| + \lim_{j \rightarrow \infty} \frac{1}{j} \sum_{l=1}^{j-1} h_l \right| = |\gamma_{\text{H}}(E_n) + \bar{h}|. \quad (12)$$

For the Bernoulli-type disorder considered in this work, the spatial average of the imaginary gauge field vanishes in the thermodynamic limit, i.e., $\bar{h} = \lim_{N \rightarrow \infty} (1/N) \sum_{l=1}^N h_l = 0$. Consequently, the Lyapunov exponent of the non-Hermitian model is asymptotically determined by that of its Hermitian counterpart: $\gamma_{\text{NH}}(E_n) \simeq \gamma_{\text{H}}(E_n)$.

This mapping allows us to determine the localization transitions using known results from the Hermitian AAH models:

(i) In the limit $J_2 = 0$, the system reduces to the standard AAH model. The Lyapunov exponent exhibits a global transition at $\lambda = 2J_1$. For $\lambda < 2J_1$, all states are extended in the Hermitian frame ($\gamma_H = 0$), implying $\gamma_{NH} = 0$ (corresponding to the fully ENHSE phase). For $\lambda > 2J_1$, all states are localized ($\gamma_H = \ln(\lambda/2J_1) > 0$), implying $\gamma_{NH} > 0$ (corresponding to the fully localized phase).

(ii) For $J_2 \neq 0$, the auxiliary Hermitian model supports an energy-dependent mobility edge E_c . As a result, the Lyapunov exponent becomes energy selective: states on one side of the mobility edge have $\gamma_H(E) > 0$ and thus $\gamma_{NH}(E) > 0$, while those on the other side satisfy $\gamma_H(E) = 0$ and hence $\gamma_{NH}(E) = 0$. This implies that the non-Hermitian system inherits a mobility-edge boundary at the same E_c , but the two sectors correspond to Anderson-localized states ($\gamma_{NH} > 0$) and ENHSE-type states ($\gamma_{NH} = 0$), respectively, rather than localized versus extended states.

Dynamical evolution

We investigate the expansion dynamics of a wave packet initially localized at the lattice center $|\Psi(0)\rangle = |j_0\rangle$ with $j_0 = N/2$ for even N , evolving under the non-Hermitian AA model defined by the Hamiltonian in Eq. (1). The time-evolved state is

$$|\Psi(t)\rangle = \frac{1}{\sqrt{\mathcal{N}(t)}} e^{-i\hat{H}t} |\Psi(0)\rangle, \quad (13)$$

where $\mathcal{N}(t)$ is the normalization factor ensuring $\langle \Psi(t) | \Psi(t) \rangle = 1$. For numerical time propagation, we discretize the evolution time t into \bar{M} steps with $dt = t/\bar{M}$. In the limit $\bar{M} \rightarrow \infty$ (*i.e.*, $dt \rightarrow 0$), keeping terms up to first order in dt , the state at time $(\bar{m} + 1)dt$ is iteratively updated as

$$|\Psi((\bar{m} + 1)dt)\rangle = \frac{(1 - i\hat{H}dt)|\Psi(\bar{m}dt)\rangle}{\sqrt{\langle \Psi(\bar{m}dt) | (1 + i\hat{H}dt)(1 - i\hat{H}dt) | \Psi(\bar{m}dt) \rangle}}, \quad (14)$$

where \bar{m} is the iteration index, and for the first step,

$$|\Psi(dt)\rangle = \frac{(1 - i\hat{H}dt)|\Psi(0)\rangle}{\sqrt{\langle \Psi(0) | (1 + i\hat{H}dt)(1 - i\hat{H}dt) | \Psi(0) \rangle}}. \quad (15)$$

After \bar{M} iterations, we obtain $|\Psi(t)\rangle$.

ACKNOWLEDGMENTS

We are grateful to Zhanpeng Lu and Hui Liu for fruitful discussions. Z. X. is supported by the NSFC (Grants No. 12375016 and No. 12461160324), Beijing National Laboratory for Condensed Matter Physics (Grant No. 2023BNL-CMPKF001). F. M is funded by the National Key Research and Development Program of China (Grant No. 2022YFA1404201) and National Natural Science Foundation of China (Grant No. 12474361). G. N. is supported by the National's Training Program of Innovation for Undergraduates (Grant No. 216972001).

DATA AVAILABILITY

The data that support the findings of this study are available from the corresponding authors upon reasonable request.

CODE AVAILABILITY

The code used for the analysis is available from the authors upon reasonable request.

AUTHOR CONTRIBUTIONS STATEMENT

Z. H. X., Z. J. L., and F. M. conceived and designed the project. N. G. L. performed the numerical simulations. Z. H. X. provided the explanation of the numerical results. All authors contributed to the discussion of the results and wrote the paper.

COMPETING INTERESTS

The authors declare no competing interests.

[1] Carl, M. B. & Stefan, B. Real spectra in non-Hermitian Hamiltonians having PT symmetry. *Phys. Rev. Lett.* **80**, 5243 (1998).

[2] Regensburger, A. et al. Parity-time synthetic photonic lattices. *Nature*(London) **488**, 167–171 (2012).

[3] Lee, T. E. Anomalous edge state in a non-Hermitian lattice. *Phys. Rev. Lett.* **116**, 133903 (2016).

[4] Takata1, K. & Notomi, M. Photonic topological insulating phase induced solely by gain and loss. *Phys. Rev. Lett.* **121**, 213902 (2018).

[5] Shuo, L. et al. Gain and loss-induced topological insulating phase in a non-Hermitian electrical circuit. *Phys. Rev. Appl.* **13**, 014047 (2020).

[6] Franca, S., Könye, V., Hassler, F., Brink, J. V. D. & Fulga, C. Non-Hermitian physics without gain or loss: The skin effect of reflected waves. *Phys. Rev. Lett.* **129**, 086601 (2022).

[7] Peng, M. et al. Acoustic non-Hermitian Dirac states tuned by flexible designed gain and loss. *Appl. Phys. Lett.* **125**, 193101 (2024).

[8] Sarkar, S., Satpathi, S. & Pati, S. K. Localization transitions in an open quasiperiodic ladder. *arXiv: 2511.08053*.

[9] Roy, S. & Maiti, S. K. Transport characteristics in Hermitian and non-Hermitian Fibonacci rings: A comparative study. *arXiv: 2601.05743*.

[10] Kunst, F. K., Edvardsson, E., Budich, J. C. & Bergholtz, E. J. Biorthogonal bulk-boundary correspondence in non-Hermitian systems. *Phys. Rev. Lett.* **121**, 026808 (2018).

[11] Ramy, E. G. et al. Non-Hermitian physics and PT symmetry. *Nat. Phys.* **14**, 11-19 (2018).

[12] Simon, L. et al. Symmetry breaking and error correction in open quantum systems. *Phys. Rev. Lett.* **125**, 240405 (2020).

[13] Liu, J. J. et al. Experimental realization of Weyl exceptional rings in a synthetic three-dimensional non-Hermitian phononic crystal. *Phys. Rev. Lett.* **129**, 084301 (2022).

[14] Kohei, K., Tokiro, N. & Shinsei, R. Entanglement phase transition induced by the non-Hermitian skin effect. *Phys. Rev. X* **13**, 021007 (2023).

[15] Chimedessa, G. F., You, J. S., Ku, H. Y. & Jen, H. H. Accelerating multipartite entanglement generation in non-Hermitian superconducting qubits. *Quantum Sci. Technol.* **10**, 025021 (2025).

[16] Zhang, L. et al. Acoustic non-Hermitian skin effect from twisted winding topology. *Nat. Commun.* **12**, 6297 (2021).

[17] Sánchez, L. H., Prieto, I. R., Eguíbar, F. S. & Cessa, H. M. M. Exact solution for the interaction of two decaying quantized fields. *Opt. Lett.* **48**, 5435-5438 (2023).

[18] Shu, X. Q. et al. Chiral transmission by an open evolution trajectory in a non-Hermitian system. *Light-Sci. Appl.* **13**, 65 (2024).

[19] Lei, Z. T., Lee, C. H. & Li, L. H. Activating non-Hermitian skin modes by parity-time symmetry breaking. *Commun. Phys.* **7**, 100 (2024).

[20] Leadbeater, C., Fitzpatrick, N., Ramo, D. M. & Thom, A. J. W. Non-unitary Trotter circuits for imaginary time evolution. *Quantum Sci. Technol.* **9**, 045007 (2024).

[21] Sounas, L. D. & Alù, A. Non-reciprocal photonics based on time modulation. *Nat. Photon.* **11**, 774–783 (2017).

[22] Gao, F. et al. Experimental demonstration of the non-Hermitian radio frequency metasurface with polarization-dependent unidirectional reflectionless propagation. *Adv. Photon. Res.* **3**, 2200019 (2022).

[23] Li, A. D. et al. Exceptional points and non-Hermitian photonics at the nanoscale. *Nat. Nanotechnol.* **18**, 706–720 (2023).

[24] Yan, Q. C. et al. Advances and applications on non-Hermitian topological photonics. *Nanophoton.* **12**, 2247–2271 (2023).

[25] Meng, H. Y., Ang, Y. S. & Lee, C. H. Exceptional points in non-Hermitian systems: Applications and recent developments. *Appl. Phys. Lett.* **124**, 060502 (2024).

[26] Gu, Z. M. et al. Observation of an acoustic non-Hermitian topological Anderson insulator. *Sci. China-Phys. Mech. Astron* **66**, 294311 (2023).

[27] Zhang, Q. C. et al. Observation of acoustic non-Hermitian Bloch braids and associated topological phase transitions. *Phys. Rev. Lett.* **130**, 017201 (2023).

[28] Zhou, H. T. et al. Underwater scattering exceptional point by metasurface with fluid-solid interaction. *Adv. Funct. Mater.* **34**, 2404282 (2024).

[29] Zhu, P. H., Sun, X. Q., Taylor, L. H. & Bahl, G. Higher rank chirality and non-Hermitian skin effect in a topoelectrical circuit. *Nat. Commun.* **14**, 720 (2023).

[30] Huang, Z. H., He, P., Lang, L. J. & Zhu, S. L. Quantum circuit for measuring an operator's generalized expectation values and its applications to non-Hermitian winding numbers. *Phys. Rev. A* **107**, 052205 (2023).

[31] Zhang, X. W. et al. Observation of continuum Landau modes in non-Hermitian electric circuits. *Nat. Commun.* **15**, 1798 (2024).

[32] Rafi-Ul-Islam, S. M., Siu, Z. B., Razo, M. S. H. & Mansoor Jalil, B. A. Critical non-Hermitian skin effect in a cross-coupled Hermitian chain. *Phys. Rev. B* **111**, 115415 (2025).

[33] Wang, Y. T. et al. Direct non-Hermitian measurement and uncertainty relation for the high-dimensional quantum domain. *Phys. Rev. Appl.* **24**, 024006 (2025).

[34] Bergholtz, E. J., Budich, J. C. & Kunst, F. K. Exceptional topology of non-Hermitian systems. *Rev. Mod. Phys.* **93**, 015005 (2021).

[35] Ramos, T., Ripoll, J. J. G. & Porras, D. Topological input-output theory for directional amplification. *Phys. Rev. A* **103**, 033513 (2021).

[36] Reisenbauer, M. et al. Non-Hermitian dynamics and non-reciprocity of optically coupled nanoparticles. *Nat. Phys.* **20**, 1629–1635 (2024).

[37] Yu, T., Zou, J., Zeng, B. W., Rao, J. W., Xia, K. Non-Hermitian topological magnonics. *Phys. Rep.* **1062**, 1–86 (2024).

[38] Zhang, B. W., Shang, C., Sun, J. Y., Gu, Z. C., & Yi, X. X. Manipulating spectral transitions and photonic transmission in a non-Hermitian optical system through nanoparticle perturbations. *Phys. Rev. A* **111**, 063702 (2025).

[39] Yago, D. V. I. R. et al. Non-reciprocal band structures in an exciton–polariton Floquet optical lattice. *Nat. Photon.* **18**, 548 (2024).

[40] Veenstra, J. et al. Non-reciprocal topological solitons in active metamaterials. *Nature(London)* **627**, 528–533 (2024).

[41] Raj, A., Ray, S. & Samal, S. S. Symmetry and topology in the non-Hermitian Kitaev chain. *arXiv: 2601.00951*.

[42] Lau, H. K. & Clerk, A. A. Fundamental limits and non-reciprocal approaches in non-Hermitian quantum sensing. *Nat. Commun.* **9**, 4320 (2018).

[43] Xu, Z. H., Huangfu, H. L., Zhang, Y. B. & Chen, S. Dynamical observation of mobility edges in one-dimensional incommensurate optical lattices. *New J. Phys.* **22**, 013036 (2020).

[44] Zhang, W. G. et al. Observation of non-Hermitian topology with nonunitary dynamics of solid-state spins. *Phys. Rev. Lett.* **127**, 090501 (2021).

[45] Lin, S. X. et al. Continuum Landau surface states in a non-Hermitian Weyl semimetal. *arXiv:2509.05138*.

[46] Longhi, S. Non-Hermitian skin effect beyond the tight-binding models. *Phys. Rev. B* **104**, 125109 (2021).

[47] Ding, K., Fang, C. & Ma, G. C. Non-Hermitian topology and exceptional-point geometries. *Nat. Rev. Phys.* **4**, 745–760 (2022).

[48] Pi, J. H., Wang, C. Y., Liu, Y. C. & Yan, Y. Q. Geometric origin of self-intersection points in non-Hermitian energy spectra. *Phys. Rev. B* **111**, 165407 (2025).

[49] Hu, M. Y., Lin, J. & Ding, K. Generalization of non-Hermitian spectral topology to hyperbolic lattices. *Commun. Phys.* **8**, 377 (2025).

[50] Liang, J. et al. Twist-induced non-Hermitian topology of exciton–polaritons. *Nat. Phys.* **22**, 151–157 (2026).

[51] León, Á. G., Ramos, T., Tudela, A. G. & Porras, D. Bridging the gap between topological non-Hermitian physics and open quantum systems. *Phys. Rev. A* **106**, L011501 (2022).

[52] Gupta, A., Kurnosov, A., Kottos, T. & Thevamaran, R. Reconfigurable enhancement of actuation forces by engineered losses in non-Hermitian metamaterials. *Extreme Mech. Lett.* **59**, 101979 (2023).

[53] Fortin, C., Wang, K. & Barnea, T. P. Topological amplification of the bosonic Kitaev chain with nonuniform loss. *Phys. Rev. B* **112**, 064208 (2025).

[54] Okuma, N., Kawabata, K., Shiozaki, K. & Sato, M. Topological origin of non-Hermitian skin effects. *Phys. Rev. Lett.* **124**, 086801 (2020).

[55] Robert, P. & Tsuneya, Y. Hinge non-Hermitian skin effect in the single-particle properties of a strongly correlated f-electron system. *Phys. Rev. B* **110**, 125114 (2024).

[56] Sonu, V. & Moon, J. P. Topological phase transitions of generalized Brillouin zone. *Commun. Phys.* **7**, 21 (2024).

[57] Li, L. H., Lee, C. H., Mu, S. & Gong, J. B. Critical non-Hermitian skin effect. *Nat. Commun.* **11**, 5491 (2020).

[58] Li, L. H., Lee, C. H. & Gong, J. b. Topological switch for non-Hermitian skin effect in cold-atom systems with loss. *Phys. Rev. Lett.* **124**, 250402 (2020).

[59] Gu, Z. M. et al. Transient non-Hermitian skin effect. *Nat. Commun.* **13**, 7668 (2022).

[60] Lin, R. J., Tai, T., Li, L. H. & Lee, C. H. Topological non-Hermitian skin effect. *Front. Phys.* **18**, 53605 (2023).

[61] Jiang, W. C., Wu, H., Li, Q. X., Li, J. & Zhu, J. J. Tunable non-Hermitian skin effect via gain and loss. *Phys. Rev. B* **110**, 155144 (2024).

[62] Kenji, S. & Masatoshi, S. General criterion for non-Hermitian skin effects and application: Fock space skin effects in many-body systems. *Phys. Rev. Lett.* **133**, 136502 (2024).

[63] Huang, X. Y., Li, Y. H., Zhang, G. F. & Liu, Y. C. Non-Hermitian skin effect and nonreciprocity induced by dissipative couplings. *Phys. Rev. A* **109**, L021503 (2024).

[64] Yoshida, T., Zhang, S. B., Neupert, T. & Kawakami, N. Non-Hermitian Mott skin effect. *Phys. Rev. Lett.* **133**, 076502 (2024).

[65] Chakradhar, R., Juana, M. & Tam, K. M. Interplay of non-Hermitian skin effect and electronic correlations in the non-

Hermitian Hubbard model via real-space dynamical mean-field theory. *Phys. Rev. B* **112**, 245137 (2025).

[66] Zhao, E. T. et al. Two-dimensional non-Hermitian skin effect in an ultracold Fermi gas. *Nature*(London) **637**, 565 (2025).

[67] Hu, Y. M. et al. Momentum-space non-Hermitian skin effect in an exciton-polariton system. [arXiv:2512.10146](https://arxiv.org/abs/2512.10146).

[68] Yao, S. Y. & Wang, Z. Edge states and topological invariants of non-Hermitian systems. *Phys. Rev. Lett.* **121**, 086803 (2018).

[69] Xiao, L. et al. Non-Hermitian bulk-boundary correspondence in quantum dynamics. *Nat. Phys.* **16**, 761-766 (2020).

[70] Xiao, Y. X., Zhang, Z. Q. & Chan, C. T. Restoration of non-Hermitian bulk-boundary correspondence by counterbalancing skin effect. *Commun. Phys.* **7**, 140 (2024).

[71] Wu, H., Yang, X. M. & Liu, H. Breakdown of non-Bloch bulk-boundary correspondence and emergent topology in Floquet non-Hermitian systems. [arXiv:2510.09193](https://arxiv.org/abs/2510.09193).

[72] Longhi, S. Probing non-Hermitian skin effect and non-Bloch phase transitions. *Phys. Rev. Res.* **1**, 023013 (2019).

[73] Yokomizo, K. & Murakami, S. Non-Bloch band theory of non-Hermitian systems. *Phys. Rev. Lett.* **123**, 066404 (2019).

[74] Jiang, H., Lang, L. J., Yang, C., Zhu, S. L. & Chen, S. Interplay of non-Hermitian skin effects and Anderson localization in nonreciprocal quasiperiodic lattices. *Phys. Rev. B* **100**, 054301 (2019).

[75] Longhi, S. Topological phase transition in non-Hermitian quasicrystals. *Phys. Rev. Lett.* **122**, 237601 (2019).

[76] Xu, Z. H., Xu, X. & Chen, S. Exact mobility edges and topological phase transition in two-dimensional non-Hermitian quasicrystals. *Sci. China-Phys. Mech. Astron.* **65**, 227211 (2022).

[77] Wang, Y. S. X., Song, D. Z., & Xia, X. Non-Hermitian mosaic Aubry-André-Harper model. *Chin. Phys. B* **34**, 090201 (2025).

[78] Zhang, Y. L. & Zhou, L. W. Two-body interaction induced phase transitions and intermediate phases in nonreciprocal non-Hermitian quasicrystals. [arXiv: 2412.11623](https://arxiv.org/abs/2412.11623).

[79] Rossignolo, M. & Anna, L. D. Localization transitions and mobility edges in coupled Aubry-André chains. *Phys. Rev. B* **99**, 054211 (2019).

[80] Cookmeyer, T., Motruk, J. & Moore, J. E. Critical properties of the ground-state localization-delocalization transition in the many-particle Aubry-André model. *Phys. Rev. B* **101**, 174203 (2020).

[81] Li, H. et al. Observation of critical phase transition in a generalized Aubry-André-Harper model with superconducting circuits. *Npj Quantum Inf.* **9**, 40 (2023).

[82] Qi, R., Cao, J. P. & Jiang, X. P. Multiple localization transitions and novel quantum phases induced by a staggered on-site potential. *Phys. Rev. B* **107**, 224201 (2023).

[83] Yi, T. C., Fang, Y. Y., Chen, W., You, W. L. & Zhang, Y. B. Unveiling quantum criticality of disordered Aubry-André-Harper models via typical fidelity susceptibility. *Phys. Rev. A* **112**, 023308 (2025).

[84] Biddle, J., Priour, D. J. J., Wang, B. & Sarma, S. D. Localization in one-dimensional lattices with non-nearest-neighbor hopping: Generalized Anderson and Aubry-André models. *Phys. Rev. B* **83**, 075105 (2011).

[85] Ramakumar, R., Das, A. N. & Sil, S. Lattice bosons in a quasi-disordered environment: The effects of next-nearest-neighbor hopping on localization and Bose-Einstein condensation. *J. Phys. A: Math. Theor.* **401**, 214-223 (2014).

[86] Weidemann, S., Kremer, M., Longhi, S. & Szameit, A. Coexistence of dynamical delocalization and spectral localization through stochastic dissipation. *Nat. Photon.* **15**, 576–581 (2021).

[87] Sahoo, H., Vijay, R. & Mujumdar, S. Anomalous transport regime in a non-Hermitian Anderson-localized hybrid system. *Phys. Rev. Res.* **4**, 043081 (2022).

[88] Balasubrahmanyam, M., Mondal, S. & Mujumdar, S. Necklace-state-mediated anomalous enhancement of transport in Anderson-localized non-Hermitian hybrid systems. *Phys. Rev. Lett.* **124**, 123901 (2020).

[89] Tzortzakakis, A. F., Makris, K. G., Szameit, A. & Economou, E. N. Transport and spectral features in non-Hermitian open systems. *Phys. Rev. Res.* **3**, 013208 (2021).

[90] Li, B., Chen, C. & Wang, Z. Universal non-Hermitian transport in disordered systems. *Phys. Rev. Lett.* **135**, 033802 (2025).

[91] André, L. Relevance of disorder for Dirac Fermions with imaginary vector potentials. *Phys. Rev. Lett.* **84**, 1292 (2000).

[92] Sascha, H., Christopher, D. W., & Gil, R. Extracting many-body localization lengths with an imaginary vector potential. *Phys. Rev. B* **103**, 064201 (2021).

[93] Midya, B. Topological phase transition in fluctuating imaginary gauge fields. *Phys. Rev. A* **109**, L061502 (2024).

[94] Cheng, J. Q., Yin, S. & Yao, D. X. Dynamical localization transition in the non-Hermitian lattice gauge theory. *Commun. Phys.* **7**, 58 (2024).

[95] Pang, Z. H., Wong, B. T. T., Hu, J. B. & Yang, Y. Synthetic non-Abelian gauge fields for non-Hermitian systems. *Phys. Rev. Lett.* **132**, 043804 (2024).

[96] Longhi, S. Magnetic control of the non-Hermitian skin effect in two-dimensional lattices. *Phys. Rev. B* **112**, 214208 (2025).

[97] Longhi, S. Erratic non-Hermitian skin localization. *Phys. Rev. Lett.* **134**, 196302 (2025).

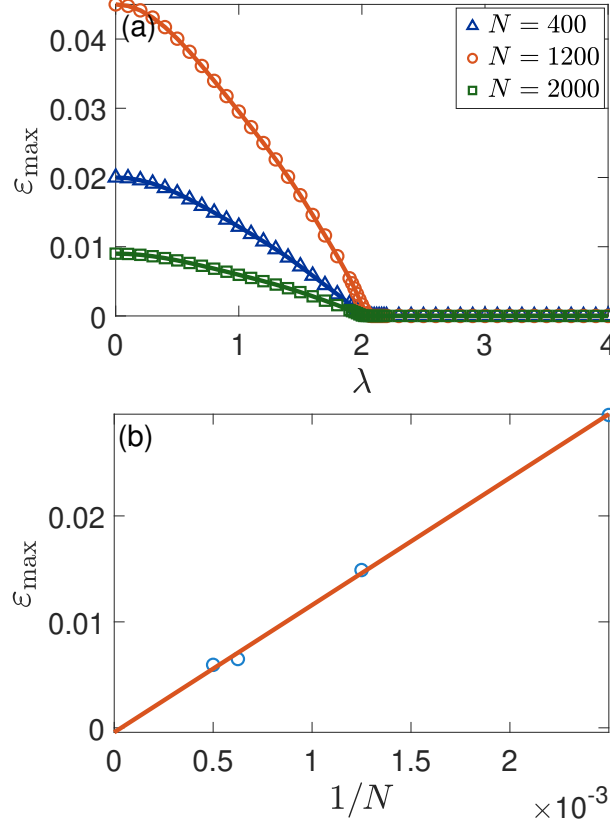


FIG. 10. (a) ε_{\max} versus λ for different N . (b) Finite-size scaling of ε_{\max} for $\lambda = 1$. Here, $J_2 = 0$ and PBCs are chosen.

APPENDIX

A. Finite-size-induced spectral complexification

For a finite system size, the spatial average of the imaginary gauge field, $\bar{h} = (1/N) \sum_{i=1}^N h_i$ generally deviates from zero for a given disorder realization. A nonzero \bar{h} introduces a residual non-Hermiticity under PBCs and thus yields finite imaginary parts in the PBC spectrum in the ENHSE regime. Consequently, the apparent spectral reality at finite N can be affected by \bar{h} .

To quantify this finite-size effect, we evaluate the maximum imaginary part of the PBC eigenenergies ε_{\max} . Figure 10(a) shows ε_{\max} as a function of λ for $J_2 = 0$ and several system sizes. In the fully ENHSE phase ($\lambda < 2$), ε_{\max} is finite at finite N but decreases systematically with increasing N . By contrast, in the fully localized phase ($\lambda > 2$), $\varepsilon_{\max} \approx 0$ and is nearly size-independent. The size scaling is further illustrated in Fig. 10(b) at a representative point $\lambda = 1$. As N increases, ε_{\max} decreases and extrapolates to $\varepsilon_{\max} \rightarrow 0$ as $N \rightarrow \infty$, confirming that the complex-valued PBC spectrum in the ENHSE phase is a finite-size effect stemming from $\bar{h} \neq 0$. Accordingly, in the thermodynamic limit where $\bar{h} \rightarrow 0$, the PBC spectrum becomes entirely real.